



Contents lists available at ScienceDirect

Nuclear Inst. and Methods in Physics Research, A

journal homepage: www.elsevier.com/locate/nima

Characterization of the Hamamatsu VUV4 MPPCs for nEXO

G. Gallina^{1,2,*}, P. Giampa¹, F. Retière¹, J. Kroeger^{1,a}, G. Zhang^{1,b}, M. Ward^{1,c}, P. Margetak¹, G. Li³, T. Tsang⁴, L. Doria^{1,d}, S. Al Kharusi⁵, M. Alfaris⁶, G. Anton⁷, I.J. Arnquist⁸, I. Badhrees^{9,e}, P.S. Barbeau¹⁰, D. Beck¹¹, V. Belov¹², T. Bhatta¹³, J. Blatchford⁶, J.P. Brodsky¹⁴, E. Brown¹⁵, T. Brunner^{1,5}, G.F. Cao^{16,f}, L. Cao¹⁷, W.R. Cen¹⁶, C. Chambers¹⁸, S.A. Charlebois¹⁹, M. Chiu⁴, B. Cleveland^{20,g}, M. Coon¹¹, A. Craycraft¹⁸, J. Dalmasson³, T. Daniels²¹, L. Darroch⁵, S.J. Daugherty²², A. De St. Croix^{1,2}, A. Der Mesrobian-Kabakian²⁰, R. DeVoe³, J. Dilling^{1,2}, Y.Y. Ding¹⁶, M.J. Dolinski²³, A. Dragone²⁴, J. Echevers¹¹, M. Elbeltagi⁹, L. Fabris²⁵, D. Fairbank¹⁸, W. Fairbank¹⁸, J. Farine²⁰, S. Feyzbakhsh⁶, R. Fontaine¹⁹, P. Gautam²³, G. Giacomini⁴, R. Gornea^{1,9}, G. Gratta³, E.V. Hansen²³, M. Heffner¹⁴, E.W. Hoppe⁸, J. Hößl⁷, A. House¹⁴, M. Hughes²⁶, Y. Ito^{5,h}, A. Iverson¹⁸, A. Jamil²⁷, M.J. Jewell³, X.S. Jiang¹⁶, A. Karelín¹², L.J. Kaufman^{22,24}, D. Kodroff⁶, T. Koffas⁹, R. Krücken^{1,2}, A. Kuchenkov¹², K.S. Kumar²⁸, Y. Lan^{1,2}, A. Larson¹³, B.G. Lenardo³, D.S. Leonard²⁹, S. Li¹¹, Z. Li²⁷, C. Licciardi²⁰, Y.H. Lin²³, P. Lv¹⁶, R. MacLellan¹³, T. McElroy⁵, M. Medina-Peregrina⁵, T. Michel⁷, B. Mong²⁴, D.C. Moore²⁷, K. Murray⁵, P. Nakarmi²⁶, R.J. Newby²⁵, Z. Ning¹⁶, O. Njoya²⁸, F. Nolet¹⁹, O. Nusair²⁶, K. Odgers¹⁵, A. Odian²⁴, M. Oriunno²⁴, J.L. Orrell⁸, G.S. Ortega⁸, I. Ostrovskiy²⁶, C.T. Overman⁸, S. Parent¹⁹, A. Piepke²⁶, A. Pocar⁶, J.-F. Pratte¹⁹, D. Qiu¹⁷, V. Radeka⁴, E. Raguzin⁴, S. Rescia⁴, M. Richman²³, A. Robinson²⁰, T. Rossignol¹⁹, P.C. Rowson²⁴, N. Roy¹⁹, R. Saldanha⁸, S. Sangiorgio¹⁴, K. Skarpaas VIII²⁴, A.K. Soma²⁶, G. St-Hilaire¹⁹, V. Stekhanov¹², T. Stiegler¹⁴, X.L. Sun¹⁶, M. Tarka⁶, J. Todd¹⁸, T. Tolba^{16,i}, T.I. Totev⁵, R. Tsang⁸, F. Vachon¹⁹, V. Veeraraghavan²⁶, G. Visser²², J.-L. Vuilleumier³⁰, M. Wagenpfeil⁷, M. Walent²⁰, Q. Wang¹⁷, J. Watkins⁹, M. Weber³, W. Wei¹⁶, L.J. Wen¹⁶, U. Wichoski²⁰, S.X. Wu³, W.H. Wu¹⁶, X. Wu¹⁷, Q. Xia²⁷, H. Yang¹⁷, L. Yang¹¹, Y.-R. Yen²³, O. Zeldovich¹², J. Zhao¹⁶, Y. Zhou¹⁷, T. Ziegler⁷

¹ TRIUMF, Vancouver, British Columbia V6T 2A3, Canada² Department of Physics and Astronomy, University of British Columbia, Vancouver, British Columbia V6T 1Z1, Canada³ Physics Department, Stanford University, Stanford, CA 94305, USA⁴ Brookhaven National Laboratory, Upton, NY 11973, USA⁵ Physics Department, McGill University, Montréal, Québec H3A 2T8, Canada⁶ Amherst Center for Fundamental Interactions and Physics Department, University of Massachusetts, Amherst, MA 01003, USA⁷ Erlangen Centre for Astroparticle Physics (ECAP), Friedrich-Alexander University Erlangen-Nürnberg, Erlangen 91058, Germany⁸ Pacific Northwest National Laboratory, Richland, WA 99352, USA⁹ Department of Physics, Carleton University, Ottawa, Ontario K1S 5B6, Canada¹⁰ Department of Physics, Duke University, and Triangle Universities Nuclear Laboratory (TUNL), Durham, NC 27708, USA

* Corresponding author at: TRIUMF, Vancouver, British Columbia V6T 2A3, Canada.

E-mail address: giacomo@triumf.ca (G. Gallina).^a Now at Physikalisches Institut der Universität Heidelberg, Heidelberg, Germany.^b Now at School of Science, Xi'an Polytechnic University, Xi'an, China.^c Now at Department of Physics, Queen's University, Kingston, Ontario, Canada.^d Now at Institut für Kernphysik, Johannes Gutenberg-Universität Mainz, Mainz, Germany.^e Also at Home institute King Abdulaziz City for Science and Technology, KACST, Riyadh 11442, Saudi Arabia.^f Also at University of Chinese Academy of Sciences, Beijing 100049, China.^g Also at SNOLAB, Ontario, Canada.^h Now at JAEA, Ibaraki, Japan.ⁱ Now at the Institut für Kernphysik, Forschungszentrum Jülich, 52428 Jülich, Germany.<https://doi.org/10.1016/j.nima.2019.05.096>

Received 25 March 2019; Received in revised form 17 May 2019; Accepted 31 May 2019

Available online 18 June 2019

0168-9002/© 2019 Elsevier B.V. All rights reserved.

¹¹ Physics Department, University of Illinois, Urbana-Champaign, IL 61801, USA¹² Institute for Theoretical and Experimental Physics named by A.I. Alikhanov of National Research Center “Kurchatov Institute”, Moscow 117218, Russia¹³ Department of Physics, University of South Dakota, Vermillion, SD 57069, USA¹⁴ Lawrence Livermore National Laboratory, Livermore, CA 94550, USA¹⁵ Department of Physics, Applied Physics and Astronomy, Rensselaer Polytechnic Institute, Troy, NY 12180, USA¹⁶ Institute of High Energy Physics, Chinese Academy of Sciences, Beijing 100049, China¹⁷ Institute of Microelectronics, Chinese Academy of Sciences, Beijing 100029, China¹⁸ Physics Department, Colorado State University, Fort Collins, CO 80523, USA¹⁹ Université de Sherbrooke, Sherbrooke, Québec J1K 2R1, Canada²⁰ Department of Physics, Laurentian University, Sudbury, Ontario P3E 2C6, Canada²¹ Department of Physics and Physical Oceanography, University of North Carolina at Wilmington, Wilmington, NC 28403, USA²² Department of Physics and CEEM, Indiana University, Bloomington, IN 47405, USA²³ Department of Physics, Drexel University, Philadelphia, PA 19104, USA²⁴ SLAC National Accelerator Laboratory, Menlo Park, CA 94025, USA²⁵ Oak Ridge National Laboratory, Oak Ridge, TN 37831, USA²⁶ Department of Physics and Astronomy, University of Alabama, Tuscaloosa, AL 35487, USA²⁷ Wright Laboratory, Department of Physics, Yale University, New Haven, CT 06511, USA²⁸ Department of Physics and Astronomy, Stony Brook University, SUNY, Stony Brook, NY 11794, USA²⁹ IBS Center for Underground Physics, Daejeon 34126, Republic of Korea³⁰ LHEP, Albert Einstein Center, University of Bern, Bern CH-3012, Switzerland

ARTICLE INFO

Keywords:

Hamamatsu

MPPCs

VUV4

SiPMs

nEXO

PDE

ABSTRACT

In this paper we report on the characterization of the Hamamatsu VUV4 (S/N: S13370-6152) Vacuum Ultra-Violet (VUV) sensitive Multi-Pixel Photon Counters (MPPC)s as part of the development of a solution for the detection of liquid xenon scintillation light for the nEXO experiment. Various MPPC features, such as: dark noise, gain, correlated avalanches, direct crosstalk and Photon Detection Efficiency (PDE) were measured in a dedicated setup at TRIUMF. MPPCs were characterized in the range $163 \text{ K} \leq T \leq 233 \text{ K}$. At an over voltage of $3.1 \pm 0.2 \text{ V}$ and at $T = 163 \text{ K}$ we report a number of Correlated Avalanches (CAs) per pulse in the $1 \mu\text{s}$ interval following the trigger pulse of 0.161 ± 0.005 . At the same settings the Dark-Noise (DN) rate is $0.137 \pm 0.002 \text{ Hz/mm}^2$. Both the number of CAs and the DN rate are within nEXO specifications. The PDE of the Hamamatsu VUV4 was measured for two different devices at $T = 233 \text{ K}$ for a mean wavelength of $189 \pm 7 \text{ nm}$. At $3.6 \pm 0.2 \text{ V}$ and $3.5 \pm 0.2 \text{ V}$ of over voltage we report a PDE of $13.4 \pm 2.6\%$ and $11 \pm 2\%$, corresponding to a saturation PDE of $14.8 \pm 2.8\%$ and $12.2 \pm 2.3\%$, respectively. Both values are well below the 24% saturation PDE advertised by Hamamatsu. More generally, the second device tested at $3.5 \pm 0.2 \text{ V}$ of over voltage is below the nEXO PDE requirement. The first one instead yields a PDE that is marginally close to meeting the nEXO specifications. This suggests that with modest improvements the Hamamatsu VUV4 MPPCs could be considered as an alternative to the FBK-LF Silicon Photo-Multipliers for the final design of the nEXO detector.

1. Introduction

Silicon Photo-Multipliers (SiPMs) have emerged as a compelling photo-sensor solution over the course of the last decade [1]. In contrast to the widely used Photomultiplier Tubes (PMTs), SiPMs are low-voltage powered, optimal for operation at cryogenic temperatures, and have low radioactivity levels with high gain stability over the time in operational conditions [2]. For these reasons, large-scale low-background cryogenic experiments, such as the next-generation Enriched Xenon Observatory experiment (nEXO) [3], are migrating to a SiPM-based light detection system [4,5]. nEXO aims to probe the boundaries of the standard model of particle physics by searching for neutrino-less double beta decay ($0\nu\beta\beta$) of ^{136}Xe [6]. This lepton number violating process would imply that neutrinos are Majorana fermions.

The photo-sensor portion of the nEXO experiment must meet the following requirements [3,7]: (i) Photon Detection Efficiency (PDE) greater than 15% for light at $174.8 \pm 10.2 \text{ nm}$ (scintillation light in liquid xenon [8]), (ii) number of correlated avalanches per pulse (within a time window of $1 \mu\text{s}$ after the trigger pulse¹) below 0.2, (iii) dark-noise rate lower than 50 Hz/mm^2 , (iv) electronic noise smaller than 0.1 Photo-electron Equivalent (PE) r.m.s. Accordingly to recent simulations the first three requirements are in fact sufficient to achieve an energy resolution of 1% for the ($0\nu\beta\beta$) decay of ^{136}Xe [7]. The last requirement is instead a combination of power consumption constraint and total

area one channel of the front-end electronics can read out [9]. In [7], it was shown that these requirements could be met with SiPMs developed by Fondazione Bruno Kessler (FBK, Trento, Italy). The latest generation of FBK SiPMs significantly exceeds nEXO requirements. The aim of this paper is to assess the performance of Hamamatsu VUV4 Multi-Pixel Photon Counters (MPPC)s (S/N: S13370-6152) developed for application in liquid xenon as a possible alternative solution to FBK SiPMs. The devices tested have a micro-cell pitch of $50 \mu\text{m}$ and an effective photosensitive area of $6 \times 6 \text{ mm}^2$. Similar characterizations for the same generation of Hamamatsu VUV4 devices, but with different series, can be found in [2,10].

2. Experimental details

2.1. Hardware setup

A setup was developed at TRIUMF to characterize the response of SiPMs at VUV wavelengths, as illustrated in Fig. 1. The measurement setup is installed in a dark box, kept under constant nitrogen gas purge and mounted on an optical platform. Humidity was monitored constantly with a HH314A Omega controller [11]. Light from a Hamamatsu L11035 xenon flash lamp [12] shines through: (i) a 1 mm diameter collimator, (ii) a VUV diffuser (Knight optical DGF1500 [13]) and (iii) a CaF₂ lens (eSource optic CF1220LCX [14]). The diffuser is placed at the focal point of the lens in order to uniformly illuminate the lens and to produce a parallel beam. The whole assembly is housed in a Radio-Frequency (RF) copper box (RF Shield #1 in Fig. 1) to shield against electromagnetic emissions from the lamp. Additionally, the VUV light passes through a set of bandpass filters, used to select the desired portion of the lamp emission spectrum and a second 1 mm

¹ In nEXO, the maximum charge integration time after the trigger will be $1 \mu\text{s}$ [3].

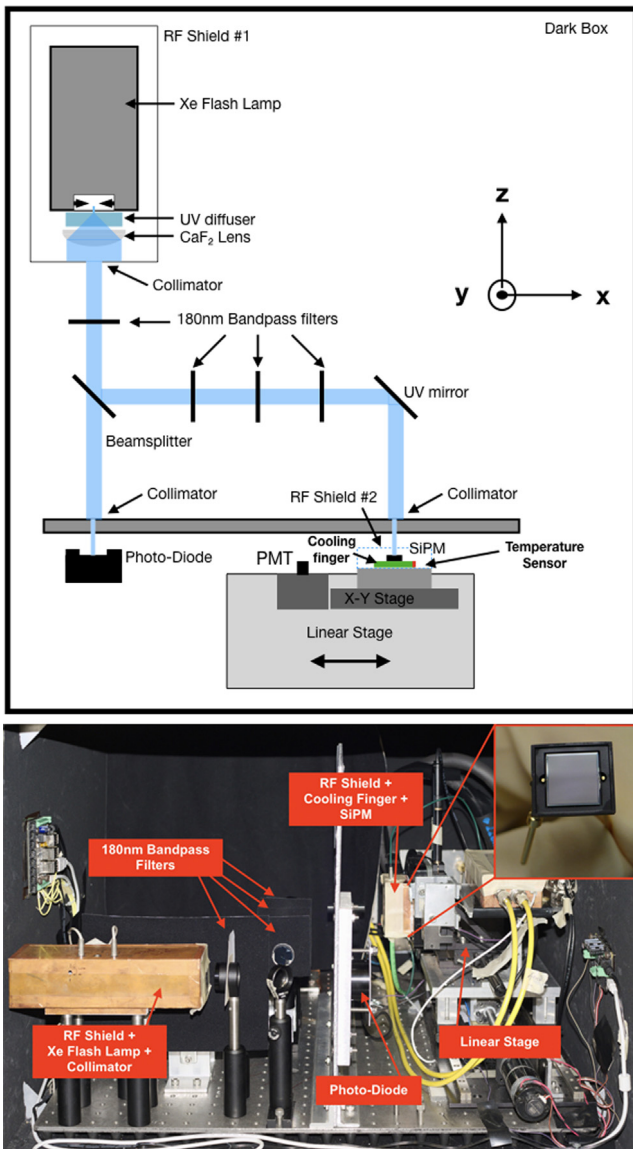


Fig. 1. Hardware setup used for the characterization of the Hamamatsu VUV4 MPPC.

diameter collimator, close to the SiPM surface (Section 2.2). Prior to filters and collimator, the light beam passes through a beam splitter, allowing to simultaneously illuminate the VUV4 MPPC and a Newport 918D-UV-OD3 Photo-Diode (PD) [15], used to monitor the xenon flash lamp light stability. The SiPM is mounted inside a second RF shielding copper box (RF Shield #2 in Fig. 1) placed on a movable optical arm which allows for remote positioning of the SiPM in the x–y plane. A liquid nitrogen controlled cold finger adjusts the temperature of the SiPM down to 163 K.² An additional UV-sensitive R9875P Hamamatsu PMT [12] is also mounted on the x–y stage and used during PDE measurements to calibrate the absolute light flux at the location of the SiPM. The SiPM and PMT can be interchanged remotely. A CAEN DT5730B Digitizer Module [16] and a MIDAS-based control system [17], are used for signal digitalization and constitute the Data Acquisition System (DAQ) of the current setup. The SiPM signal is amplified by two MAR6-SM+ amplifiers in series [18]. The acquisition trigger module, the PD controller, the filters controller, the x–y stage controller, the PMT and the SiPM power supply are all placed outside the dark box.

² The temperature stability was found to be ± 1 K.

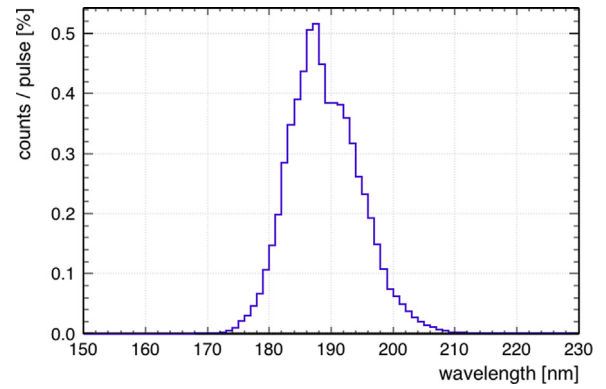


Fig. 2. Filtered xenon flash lamp spectrum measured after application of the 4 VUV filters. The shoulder effect around 190 nm is due to the combination of the original xenon flash lamp spectrum and the different filters transmissions.

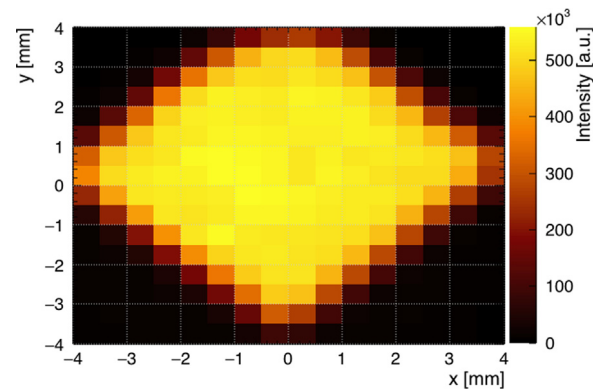


Fig. 3. Position mapping of the VUV beam at the SiPM location. The SiPM was moved in the x and y coordinates of Fig. 1 at increments of 0.5 mm in each direction.

2.2. Light filtering scheme

A set of 4 narrow bandpass filters with transmission nominally centered at 180 nm selects the desired portion of the lamp emission spectrum and attenuates the xenon flash lamp light intensity. Two of the filters are 25180FNB from eSource OPTICS [14] and two are 180-NB-1D from Pelham Research Optical LLC [19]. The typical peak transmission of these filters at 180 nm is on the order of 20%. In order to establish the transmitted wavelength distribution, each filter was characterized using a VUV spectrometer (Resonance TR-SES-200 [20]). The filtered spectrum is shown in Fig. 2. It has a mean wavelength of 189 nm and a Full Width Half Maximum (FWHM) of 13 nm.

2.3. Beam position mapping

The VUV4 MPPC and the PMT, used for absolute light calibration, have different Photosensitive Areas (PA) of 6×6 mm² and 50.24 mm², respectively. For the PDE calculations it is usually necessary to normalize SiPM and PMT measurements by their photosensitive areas. This correction can be neglected if the cross section of the impinging beam is smaller than the SiPM and PMT photosensitive areas. To verify this condition, the collimated light beam was mapped with respect to the surface of the SiPM, the smaller of the two sensors. This beam map was achieved by moving the SiPM in the x–y plane (Fig. 1) in increments of 0.5 mm, and by measuring (noise subtracted) the counting rates detected by the device at each position. A typical beam-map for the SiPM is shown in Fig. 3. To size the diameter of the beam: d_{BEAM} , at the SiPM and PMT location, the x and y projections of the beam map are compared with a Monte-Carlo model (MC). Based on the collimator

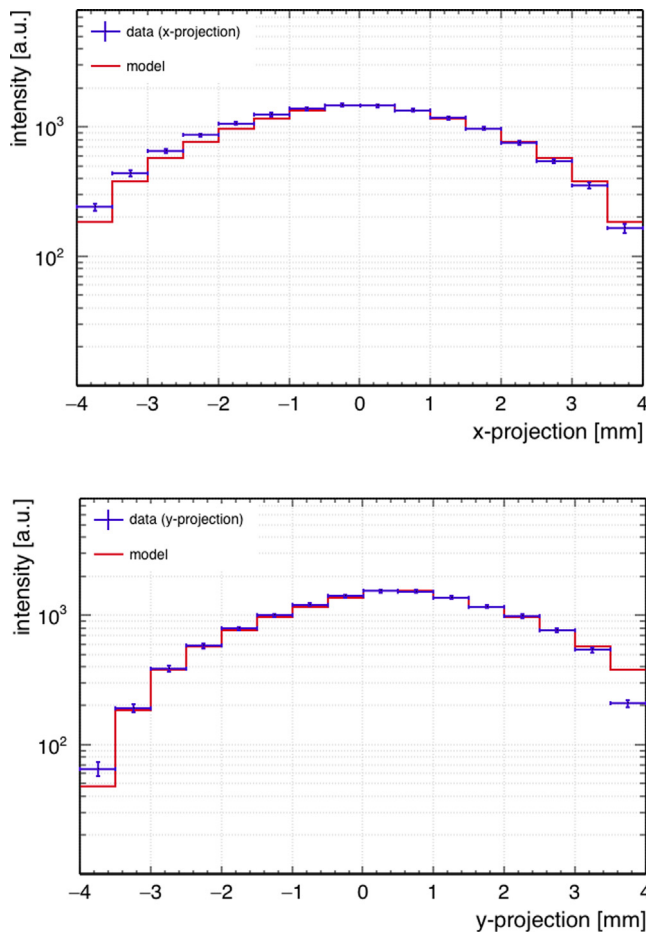


Fig. 4. Comparison between the measured beam map x–y projections (Blue) and the Monte Carlo model (Red) for the x-projection (Top) and y-projection (Bottom) of the beam map of Fig. 3. The beam diameter was estimated to be 1.2 ± 0.2 mm at the SiPM and PMT location, indicating that the beam cross-section is smaller than the SiPM and PMT photon-sensitive surface area. The χ^2 test for the two projections gives respectively a χ^2/NDF of 1.48 for the x projection and a χ^2/NDF of 1.24 for the y projection where NDF is the Number of Degree of Freedom. The biggest deviation between the model and the measurements is evident for points at the edge of the SiPM, where the relative error of the measurement increases due to a worsening of the signal to noise ratio.

size and shape, described in Section 2.1 and Fig. 1, the beam map should be the convolution between a circular beam and a square SiPM whose response in the MC model is assumed uniform across its surface. Different x and y profiles were created by letting d_{BEAM} float, and a likelihood method was used to determine the combination that best fit the data, shown in Fig. 4. The best fit beam diameter at the SiPM (or PMT) location is 1.2 ± 0.2 mm. This result confirms that: (i) the beam cross-section is smaller than the SiPM and PMT photon-sensitive areas and therefore an area correction can be neglected during efficiency measurements, (ii) the SiPM response is uniform across its surface.

2.4. Collected data and trigger configurations

The VUV4 MPPC characteristics, as a function of the temperature, were investigated in the range $163 \text{ K} \leq T \leq 233 \text{ K}$. The collected data can be divided into two types: dark data, where the SiPM was shielded from any light source, and xenon flash lamp data. For dark measurements (Sections 3.2–3.4) the SiPM copper box (RF shield # 2 in Fig. 1) was closed, enabling data-collection at temperatures below 233 K. The DAQ system was set to trigger on individual SiPM pulses with a DAQ threshold above the noise. For each trigger, the DAQ saves the event with a total sample window of 20 μs , split into 4 μs of pre-trigger

and 16 μs of post-trigger samples. The long post-trigger window is necessary in order to measure delayed correlated pulses, while the long pre-trigger window ensures that no tail from previous pulses persists. Dark data were collected at different temperatures and over voltages. For xenon flash lamp data (PDE measurements in Section 3.5), the DAQ was externally triggered by pulses from a waveform generator which also fired the xenon flash lamp. Furthermore, the SiPM RF shielding box was opened, allowing light to reach the SiPM. PDE measurements were performed at 233 K to prevent residual water vapor condensation. The external trigger had a frequency of 500 Hz.

3. Experimental results

3.1. Signal pulse fitting procedure

The collected dark data were analyzed at the pulse level in order to resolve individual PE pulses. A ROOT-based [21] waveform analysis toolkit was developed, similar to the one reported in [22]. See Fig. 5.

The implemented algorithm relies on a χ^2 minimization to identify and fit SiPM pulses. The Single Avalanche Response Function (SARF) was parametrized using the following equation, which accounts for the presence of two time constants in the SiPM pulse shape [23]:

$$V(t) = A \times \left[\frac{1-k}{\tau_S} \left(e^{-\frac{t-t_0}{\tau_S+\tau_R}} - e^{-\frac{t-t_0}{\tau_R}} \right) + \frac{k}{\tau_L} \left(e^{-\frac{t-t_0}{\tau_L+\tau_R}} - e^{-\frac{t-t_0}{\tau_R}} \right) \right] \quad (1)$$

where: τ_R is the pulse rise time, A is the pulse area (proportional to the pulse charge, see Section 3.2), t_0 is the pulse time, τ_S and τ_L are the short and long pulse fall time constants, respectively. k is the relative contribution of the two fall time components in the SiPM pulse shape: $0 \leq k \leq 1$. For each over voltage and temperature the collected dark pulses were fitted in a multistage algorithm. First, a pulse-finding algorithm identifies and fits single avalanche pulses to extrapolate the average SARF parameters (τ_R , τ_S , τ_L and k), according to Eq. (1). The SiPM pulse shape is then set by fixing these parameters to their estimated average values. Finally a second fit iteration is performed with fixed pulse shape to improve the estimation of pulse time and area. For fits exceeding a certain threshold of reduced χ^2 , test pulses are added iteratively to the fit. The new pulse combination is kept permanently if the reduced χ^2 of the new fit improves significantly. Else, the test pulses are discarded. The last step of the algorithm improves the capability to identify overlapping pulses (more details in [7,24]). As an example, we report in Fig. 6 the charge distribution of first pulses following single PE primary pulses (also called trigger or prompt pulses) as a function of the time difference with respect to their primary pulse recorded at $T = 163 \text{ K}$ and for an over voltage of $5.1 \pm 0.2 \text{ V}$.

3.2. Single PE gain and breakdown voltage extrapolation

Single PE dark pulses were used to measure the single PE SiPM gain as a function of the SiPM temperature. The single PE (amplified) pulse charge Q can be defined as:

$$Q \equiv \left(\frac{\text{IDR}}{2^{14}} \right) \times \left(\frac{\bar{A}_{1 \text{ PE}} \times 10^{-9}}{R} \right) \quad (2)$$

where: IDR is the input dynamic range of the digitizer (0.5 V), $\bar{A}_{1 \text{ PE}}$ is the average area (Eq. (1)) of the fitted digitizer signals for 1 PE pulses (measured in $\text{LSB} \times \text{ns}$ [16]), and R is the amplifier load resistance ($R=50 \Omega$). Therefore the single PE (un-amplified) gain $G_{1 \text{ PE}}$, can be extracted from Q using the following equation:

$$G_{1 \text{ PE}} = \frac{Q}{g_{\text{AMP}} \times q_E} \quad (3)$$

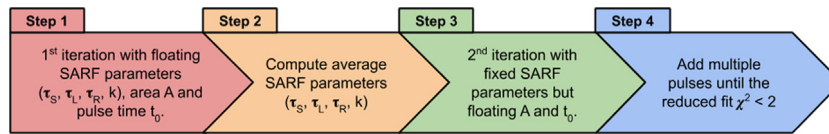


Fig. 5. Schematic representation of the waveform analysis toolkit developed for this paper. See text for a detailed explanation.

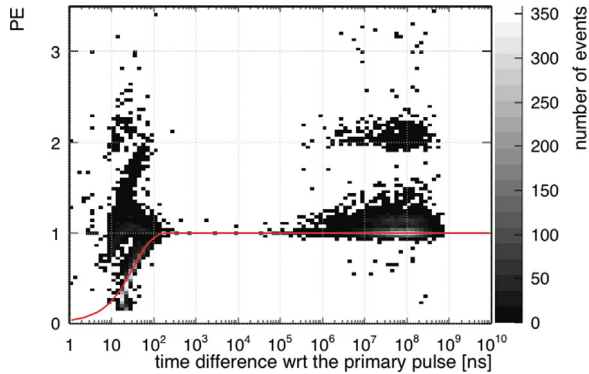


Fig. 6. Charge distribution (normalized to the average charge of 1 PE pulses) of first pulses following single PE trigger pulses as a function of the time difference with respect to (wrt) their primary pulse for $T = 163$ K and for an over voltage of 5.1 ± 0.2 V. The gray scale represents the number of events in each bin on a logarithmic scale. The solid red line shows a fit of the afterpulsing events [25] and is used to measure the recovery time of one cell, equal to 35 ± 4 ns. For a detailed explanation of the different correlated avalanche mechanisms presented in this figure, we refer the reader to [7].

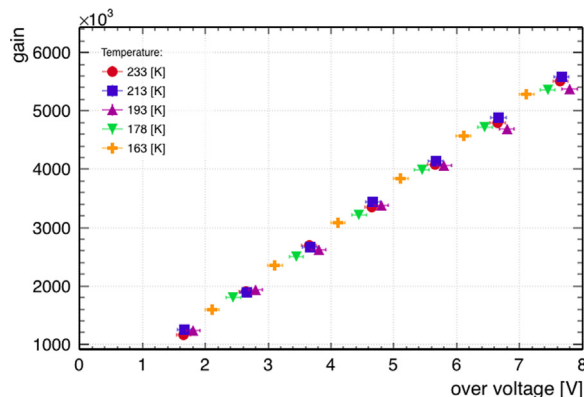


Fig. 7. Measured single PE gain (Eq. (3)) as a function of the over voltage for different SiPM temperatures.

where g_{AMP} is the gain of the amplifier (measured to be 142 ± 2)³ and q_E is the electron charge. In agreement with [26], the gain was found to increase linearly with the bias voltage V with a measured gradient of $(72.4 \pm 3.7) \times 10^4 \frac{1}{V}$. From the single PE gain it is possible to extrapolate the single PE (un-amplified) charge defined as $Q_{1\text{ PE}} \equiv q_E \times G_{1\text{ PE}}$. The single PE (un-amplified) charge, as a function of the bias voltage, was then linearly fitted as $Q_{1\text{ PE}} = C_D \times (V - V_{BD})$, in order to extract: (i) the single SiPM cell capacitance C_D and (ii) the Breakdown Voltage V_{BD} defined as the bias voltage at which the SiPM single PE gain (or charge) is zero. The breakdown voltage is found to linearly depend on the SiPM temperature with a measured gradient of

³ The amplifier gain was computed by applying a step voltage to a precision capacitor in order to inject a known charge into the SiPM amplifier input (*i.e.* Q_{IN}). The output charge was then computed from the digitized amplifier output waveform (*i.e.* Q_{OUT}). The amplifier gain follows as the ratio between the final integrated charge and the input known charge as $g_{AMP} = \frac{Q_{OUT}}{Q_{IN}}$.

$50 \pm 2 \frac{\text{mV}}{\text{K}}$. At 163 K it is measured to be $V_{BD} = 44.9 \pm 0.1$ V. The average cell capacitance, extrapolated from the fit, is $C_D = 116 \pm 6$ fF with no observed temperature dependence in the analyzed temperature range. Moreover, the total SiPM capacitance was measured using a capacitance meter (Wayne Kerr 6440B [27]), with an extracted single cell capacitance of $C_D = 104 \pm 10$ fF. The gain measurements are shown in Fig. 7 as a function of the over voltage for different SiPM temperatures.

3.3. Prompt pulse charge distribution

The pulse-charge distribution was studied using dark data and prompt pulses⁴ with the SiPM set at different over voltages and temperatures. The single (and multi) PE charge response of prompt pulses follows the shape of a Gaussian distribution, where the width of the distribution corresponds to the charge resolution combination of the electronic noise and SiPM gain fluctuations. However, we have observed that all the charge peaks show a shoulder-like component to the right of the expected Gaussian charge distribution. This feature is observed to be highly dependent on over voltage, as shown in Fig. 8 for $T = 233$ K and 163 K. The shape of the shoulder and its dependence on over voltage were further investigated. We observed that the shape of the pulses which are contributing to the shoulder is consistent with that of single PE with a higher integrated charge. Based on these observations this feature could arise from fast (<4 ns) correlated avalanches which do not get resolved from their parent primary pulse by the DAQ system. This effect could also be explained by a discrepancy in gain between micro-cells in the device.

3.4. Noise analysis

Dark and correlated avalanche noise are among the crucial parameters that characterize SiPMs. Dark Noise pulses (DN) are charge signals generated by the formation of electron-hole pairs due to thermionic or field enhanced processes [28]. The DN rate as a function of the applied over voltage for different SiPM temperatures is presented in Section 3.4.2. Correlated Avalanche (CA) noise is due to at least two processes: the production of secondary photons during the avalanche in the gain amplification stage detected in nearby cells, and the trapping and subsequent release of charge carriers produced in avalanches. The latter process is usually referred to as afterpulsing, while the former is usually called crosstalk. Crosstalk photons produce nearly simultaneous avalanches to the primary one (Direct CrossTalk (DiCT)) or delayed by several ns (Delayed CrossTalk (DeCT)) [29]. In general, the subset of the CAs constituted by afterpulses and delayed crosstalk events is named Correlated Delayed Avalanches (CDAs). Unlike DN events, CAs (and therefore CDAs) are correlated with a primary signal. In nEXO the maximum charge integration time after the trigger pulse will be 1 μ s. The number of CAs and CDAs per primary pulse in this time window as a function of the applied over voltage for different SiPM temperatures, is reported in Sections 3.4.1 and 3.4.2, respectively. Direct crosstalk is discussed in Section 3.4.3. It is worth recalling that the SiPM noise was studied using dark data, taken with the SiPM shielded from any light source (Section 2.4).

⁴ We define a prompt pulse as the first SiPM pulse in each waveform recorded by the DAQ.

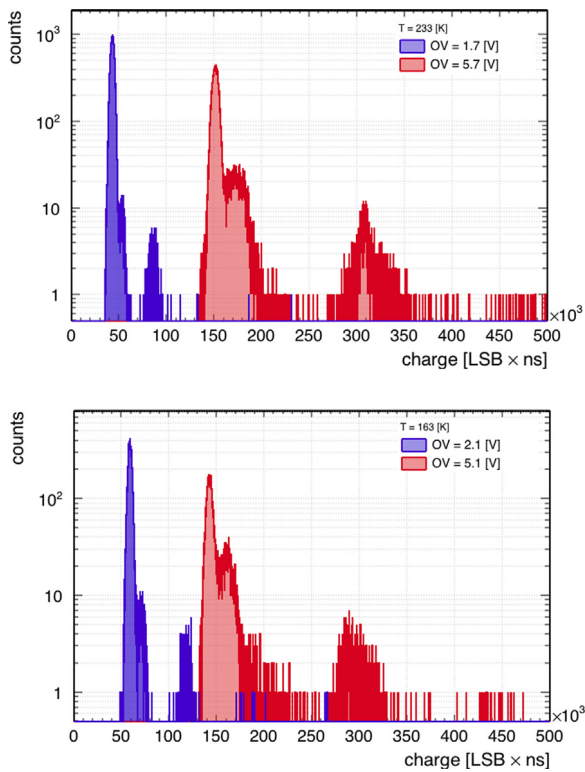


Fig. 8. Charge distribution for prompt pulses obtained using dark data for different SiPM temperatures and over voltages (Top: $T = 233$ K. Bottom: $T = 163$ K). All the charge peaks show a shoulder-like component to the right of the expected Gaussian charge distribution. This feature appears to be highly dependent on the over voltage.

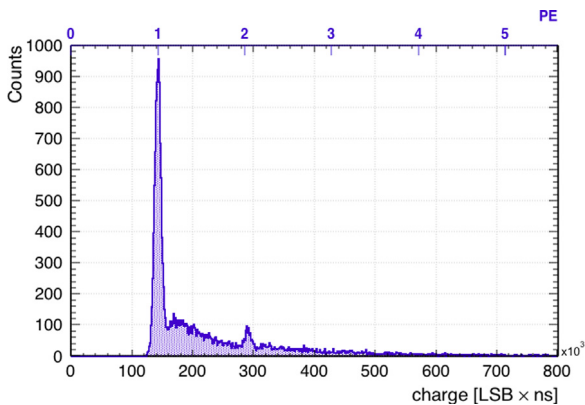


Fig. 9. Histogram of the baseline subtracted integral of collected dark waveform for an over voltage setting of 5.1 ± 0.2 V and a temperature of 163 K. Each waveform recorded by the DAQ is integrated in the range $[0-5]$ μ s. The trigger pulse is at 4 μ s and no pulses are present in the pre-trigger region ($[0-4]$ μ s). The edge next to the 1 PE Gaussian peak is a combination of shoulder-like events (as reported in Fig. 8) and waveform with after-pulses.

3.4.1. Number of correlated avalanches per pulse

In order to reach the nEXO design performance, the number of CAs per primary pulse must be below 0.2, within a time window of 1 μ s after the primary pulse. A higher value would result in worsened energy resolution [7]. The average number of CAs per pulse is measured by directly constructing a histogram of the baseline subtracted integral of collected dark waveform in the range $[0-5]$ μ s and normalizing it to the average charge of 1 PE pulses, as discussed in [7] (An example is reported in Fig. 9). In the absence of correlated noise, the mean of this histogram should be exactly 1. However, each avalanche has a non-zero probability of being accompanied by correlated avalanches

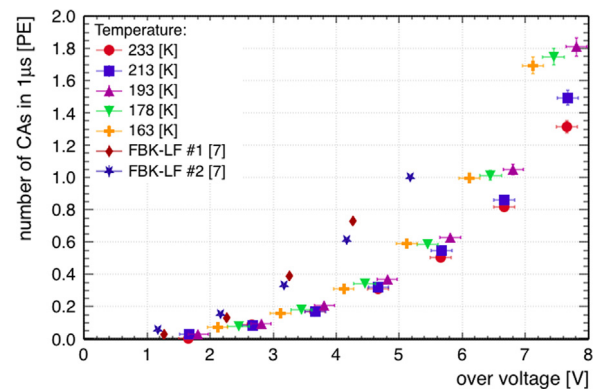


Fig. 10. Number of Correlated Avalanches (CAs) per primary pulse within a time window of 1 μ s after the trigger pulse as a function of the applied over voltage for different SiPM temperatures. FBK-LF #1 and #2 are instead the number of CAs per pulse, always in a time window of 1 μ s after the trigger pulse, reported in [7], for two FBK-LF SiPMs.

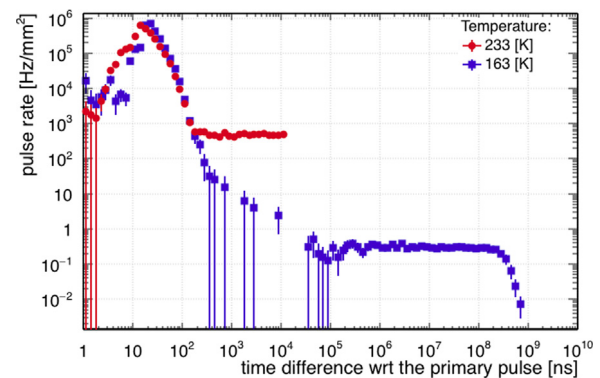


Fig. 11. Observed pulse rate $R(t)$ normalized by the SiPM photon sensitive area as a function of the time difference with respect to (wrt) the primary pulse for a temperature of 163 K (5.1 ± 0.2 V of over voltage) (Blue) and 233 K (5.7 ± 0.2 V of over voltage) (Red). At 233 K, to avoid ADC dead time corrections due to the high self trigger DN rate, the time differences were computed only between pulses inside the same DAQ window (maximum time difference: 16 μ s).

causing the mean of the waveform integral histogram to be larger than unity. The excess from unity can be then used to measure (in unit of PE) the average number of CAs per pulse in the 1 μ s interval after the trigger pulse: N_{CA} . The N_{CA} number is reported in Fig. 10, for different SiPM temperatures and over voltages. At low over voltages N_{CA} does not show an evident temperature dependence; a minor deviation is, however, observed at higher over voltages. Similar trends are reported for other SiPMs by other investigations [30]. In order to meet the nEXO requirements (Section 1), the Hamamatsu VUV4 can be operated at $T=163$ K up to 4 V of over voltage keeping N_{CA} smaller than 0.2. For comparison, in Fig. 10, we have also reported the average number of CAs per pulse of another SiPM produced specifically for nEXO by FBK, the FBK Low-Field (LF) SiPM (FBK-LF #1 and FBK-LF #2 in Fig. 10), characterized in a previously reported work [7]. The Hamamatsu VUV4 has a considerably lower N_{CA} than FBK-LF. It can therefore be operated at higher OV (i.e. higher gain) while meeting nEXO requirements ($N_{CA} \leq 0.2$). For reference, at $T=163$ K and at 3.1 ± 0.2 V of over voltage we measure $N_{CA} = 0.161 \pm 0.005$ for the Hamamatsu VUV4,⁵ while the FBK LF #1 and #2 at $T = 168$ K and 3.26 V and 3.17 V have a N_{CA} equal to 0.39 and 0.33, respectively.

⁵ 3.1 ± 0.2 V is the closest measured points for which the requirement on N_{CA} is satisfied. At this over voltage and temperature the electronics noise was measured to be 0.064 PE.

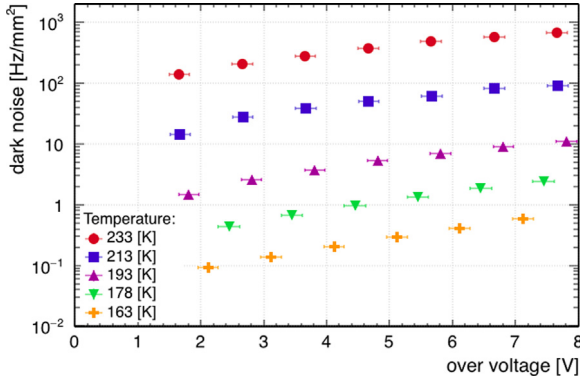


Fig. 12. Dark Noise (DN) rate normalized by the SiPM photon sensitive area as a function of the applied over voltage for different SiPM temperatures.

3.4.2. Dark noise rate and number of correlated delayed avalanches per pulse

DN and CDAs events can be distinguished by studying the time distribution of events relative to the primary pulse using a method, described in [31], that requires the charge of the primary pulse to be a single PE equivalent. The observed pulse rate $R(t)$ is then computed as a function of the time difference t from the primary pulse ($t = 0$) as:

$$R(t) = R_{\text{DN}}(t) + R_{\text{CDA}}(t) \quad (4)$$

where R_{DN} is the rate of dark noise pulses and R_{CDA} is the rate of the CDAs per pulse. An example of the measured time distribution for a given over voltage and for two different temperatures is reported in Fig. 11. The DN rate can then be estimated from Fig. 11 performing a weighted mean of the asymptotic rate at long times.⁶ The measured DN rates, for different SiPM temperatures, are shown in Fig. 12 as a function of the over voltage. For the same temperature and OV setting reported in Section 3.4.1 (163 K, 3.1 ± 0.2 V of OV), the DN rate is measured to be 0.137 ± 0.002 Hz/mm², which satisfies nEXO requirements (Section 1). By applying Eq. (4) to the observed pulse rate (e.g. Fig. 11), it is possible to compute the expected number of CDAs under a fixed time window of length Δt after the trigger pulse as:

$$N_{\text{CDA}}(\Delta t) = \int_0^{\Delta t} (R(t) - R_{\text{DN}}(t)) dt \quad (5)$$

where R_{DN} is the measured DN rate as reported in Fig. 12. The measured average number of CDAs per pulse in the $1 \mu\text{s}$ window after the trigger pulse, for different SiPM temperatures and over voltages is reported in Fig. 13. For 163 K and 3.1 ± 0.2 V of OV, the average number of CDAs per pulse in $1 \mu\text{s}$ is 0.178 ± 0.003 . Finally, it is worth noting that the number of CDAs, extrapolated in this section, cannot be compared directly with the number of CAs (Section 3.4.1). The number of CDAs is in fact derived, accordingly to [31], considering only the time differences of delayed events with respect to their primary pulse while the number of CAs accounts instead also for their different charge.

3.4.3. Number of additional prompt avalanches

Based on the measured dark noise rate reported in Section 3.4.2, and assuming Poisson statistics, the probability of having two dark noise pulses occurring within few nano-seconds is negligible. Therefore, the collected dark data can be used to investigate Direct CrossTalk (DiCT). DiCT occurs when photons generated during a triggered avalanche in one micro-cell promptly travel to the amplification region of neighboring micro-cells, where they induce a secondary avalanche. This

⁶ Each point in the mean was weighted with its error derived as reported in [31].

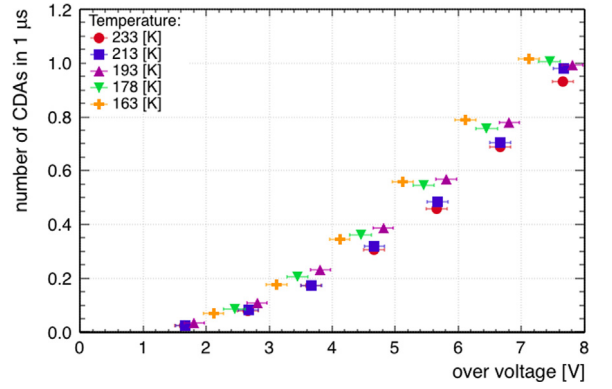


Fig. 13. Number of Correlated Delayed Avalanches (CDAs) per primary pulse within a time window of $1 \mu\text{s}$ after the trigger pulse as a function of the applied over voltage for different SiPM temperatures.

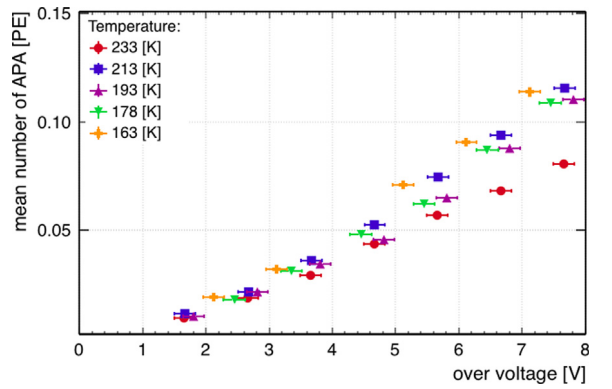


Fig. 14. Number of Additional Prompt Avalanches (APAs) as a function of the over voltage for different SiPM temperatures.

mechanism happens over pico-seconds [29] and it mimics a multiple PE signal, thus biasing the photon counting ability of the device. The charge distribution of the prompt pulses obtained from the dark data (Section 3.3) can be used to determine the mean number of Additional Prompt Avalanches (APA)s, N_{APA} , due to Direct CrossTalk :

$$N_{\text{APA}} = \frac{1}{N} \sum_{i=1}^N \frac{A_i}{\bar{A}_{1 \text{ PE}}} - 1 \quad (6)$$

where A_i is the charge of the prompt pulse i (Section 3.1), $\bar{A}_{1 \text{ PE}}$ is the average charge of 1 PE pulses and N is the number of prompt avalanches analyzed. The N_{APA} number, in unit of PE, as a function of the over voltage and for different SiPM temperatures, is reported in Fig. 14. For 163 K and for 3.1 ± 0.2 V of OV we measure a mean number of additional prompt avalanches, due to direct cross talk, equal to 0.032 ± 0.001 . The small amount of N_{APA} can also be understood looking at Fig. 6 and Fig. 9 where 3 PE events are greatly suppressed.

3.5. Photon detection efficiency

To meet nEXO requirements, the SiPM PDE must be $\geq 15\%$ [7] for liquid xenon scintillation wavelengths (174.8 ± 10.2 nm [8]). In this paper, the PDE was measured using a filtered pulsed xenon flash lamp enabling measurements free from correlated avalanches [25]. As shown in Section 2.2, the mean wavelength after filtering is 189 ± 7 nm. The generated flash pulse has a width $\sim 1 \mu\text{s}$, which prevents room temperature measurements, as the dark noise would overwhelm the light signal. For this reason PDE data were taken with the SiPM temperature set at 233 K. The PDE was measured using an experimental technique

similar to the one described in [25]. The light flux was assessed using a calibrated PMT (Section 2.1) with no corrections applied for the different photosensitive areas of the two devices (Section 2.3). The average number of photons detected by the SiPM ($\mu_{\gamma}^{\text{SiPM}}$) was measured by counting the number of lamp flashes in which no pulses were detected (N_0). Using Poisson statistics $\mu_{\gamma}^{\text{SiPM}}$ can be expressed as:

$$\mu_{\gamma}^{\text{SiPM}} = -\ln\left(\frac{N_0}{N_{\text{TOT}}}\right) - \mu_{\text{DN}} \quad (7)$$

where N_{TOT} is the total number of lamp flashes. This method is independent of correlated avalanches and it requires only correcting for the average number of dark noise pulses in the trigger window (μ_{DN}). The same analysis was applied to the reference PMT (Hamamatsu R9875P, Section 2.1) in order to measure the average number of photons detected by the PMT ($\mu_{\gamma}^{\text{PMT}}$) and then extrapolate, using the PMT Quantum Efficiency (QE) and Collection Efficiency (CE), the effective number of photons produced by the pulsed xenon flash lamp at the SiPM and PMT surface: N_{γ} . The PMT QE expresses the probability of photon–electron emission when a single photon strikes the PMT photocathode [32]. The QE reported by Hamamatsu for this phototube is $16.5 \pm 2.1\%$. The PMT CE expresses the probability that the generated photon–electron will land on the effective area of the first PMT dynode and start the amplification process [32]. The CE of this phototube was determined by Hamamatsu to be 71% without any estimate of the uncertainty. Conservatively, in agreement with [7], we assume a 10% error for the CE of this PMT (i.e. $71 \pm 10\%$) to account for the non-uniformity of the photon collection at the photo-cathode. The number of incident photons N_{γ} on the PMT surface can then be obtained as:

$$N_{\gamma} = \left(\frac{\mu_{\gamma}^{\text{PMT}}}{\text{CE} \times \text{QE}}\right) \quad (8)$$

The SiPM PDE is in turn obtained as:

$$\text{PDE}_{\text{SiPM}} = \left(\frac{\mu_{\gamma}^{\text{SiPM}}}{N_{\gamma}}\right) \quad (9)$$

The measured PDE as a function of the over voltage is shown in Fig. 15 for two different VUV4 devices labeled VUV4 #1 and VUV4 #2. VUV4 #2 is the device for which DN, CAs, CDAs and APAs are reported in the previous sections of this paper. The measured saturation PDE for VUV4 #2 and VUV4 #1 are $14.8 \pm 2.8\%$ and $12.2 \pm 2.3\%$, respectively. For comparison, we measured the PDE of one FBK LF (FBK LF # 3 in Fig. 15), for which the saturation PDE was measured to be $22.8 \pm 4.3\%$, in agreement with [7] (FBK-LF #1 and #2 in Fig. 15, see Section 3.4.1). It is important to mention that different sources of systematic uncertainty were considered and investigated for this measurement. The PMT gain stability was found to be a negligible source of uncertainty. The stability of the light flux, monitored with a photo-diode (Section 2.1), was also found to have a negligible effect, with fluctuations within 1%. The dominant source of systematic uncertainty is therefore the uncertainty on the PMT CE.

We conclude this section by interpreting the results of the PDE measurement in the context of the nEXO experiment. There are three main differences between the experimental condition of this study and the nEXO environment: (i) wavelength, (ii) angle of incidence of the light, and (iii) temperature. Firstly, as shown in Section 2.2, the filtered wavelength distribution presented in this work is about 10 nanometers higher than liquid xenon scintillation. In [33] Hamamatsu reports little wavelength dependence in this range. Secondly, as shown in Section 2.3, the angular distribution of photons at the SiPM location in the TRIUMF setup is normal to the SiPM surface. This is not the case for nEXO, for which preliminary GEANT4 optical simulations [34] show an average deviation from a normal distribution at the SiPM surface. The photon detection efficiency is likely to be lower at higher incidence angles due to increased reflectivity [25]. Finally, as explained in Section 2, the VUV4 PDE is measured at 233 K instead of liquid xenon temperature, which may affect the total PDE [35,36]. Measurements of

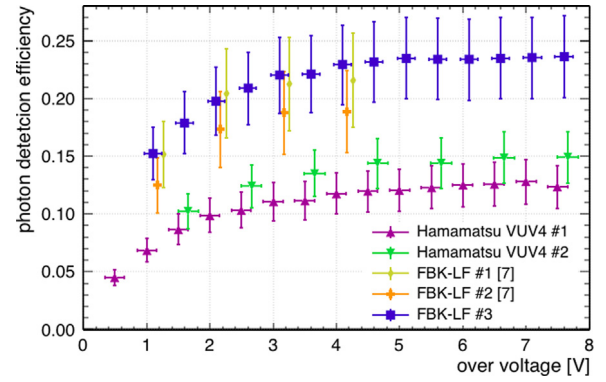


Fig. 15. Photon Detection Efficiency (PDE) as a function of the over voltage for two Hamamatsu VUV4 MPPCs and three FBK-LF SiPMs. The Hamamatsu MPPC used throughout this paper is the VUV4 #2. The FBK-LF #3 is a new FBK LF SiPM measured, for comparison, in the setup reported in this paper. FBK-LF #1 and #2 are instead the FBK-LF PDE reported in [7], whose number of CAs is reported in Section 3.4.1 and Fig. 10. The error, on each point, for all the five devices accounts for the presence both to the statistical and the systematic uncertainty.

Table 1

Summary of the results derived for the characterization of the Hamamatsu VUV4 MPPC useful for nEXO operation. The dark noise rate, the number of Correlated Avalanches (CAs) per pulse in the $1\mu\text{s}$ following the trigger pulse, the number of Additional Prompt Avalanches (APAs) and the number of Correlated Delayed Avalanches (CDAs) per pulse in the same time window are reported for a temperature of 163 K and at 3.1 ± 0.2 V of Over Voltage (OV). The Photon Detection Efficiency (PDE) was measured for two Hamamatsu VUV4 devices (labeled as VUV4 #2 and VUV4 #1) at $T = 233$ K, for a mean wavelength of 189 ± 7 nm and at an over voltage of 3.6 ± 0.2 V and 3.5 ± 0.2 V, respectively.

Quantity	Value	Unit
Dark noise rate	0.137 ± 0.002	Hz/mm ²
Number of CAs	0.161 ± 0.005	PE
Number of APAs	0.032 ± 0.001	PE
Number of CDAs	0.178 ± 0.003	–
PDE VUV4 #2	$13.4 \pm 2.6\%$	–
PDE VUV4 #1	$11 \pm 2\%$	–

SiPM reflectivity to VUV light as a function of photon incident angle and wavelength are being planned with setups properly customized to perform PDE measurements down to 163 K. These custom setups will allow us to measure the VUV4 PDE in conditions closer to those in nEXO. A lower systematic uncertainty on the VUV4 PDE will be also achieved substituting the calibrated Hamamatsu PMT with a calibrated NIST photodiode considering the smaller systematic uncertainty on the provided responsivity in the VUV range [37] if compared with the PMT CE.

4. Conclusions

This paper describes measurements performed at TRIUMF to characterize the properties of VUV sensitive SiPMs at cryogenic temperatures. In particular, this work focused on the Hamamatsu VUV4 MPPC, identified as a possible option for the nEXO experiment. The results of the characterization are summarized in Table 1. For a device temperature of 163 K, the VUV4 dark noise rate is 0.137 ± 0.002 Hz/mm² at 3.1 ± 0.2 V of over voltage, a level comfortably lower than what required for nEXO (<50 Hz/mm²). At the same over voltage setting and temperature, we measure: a number of additional prompt avalanches equal to 0.032 ± 0.001 , a number of correlated delayed avalanches per pulse in the $1\mu\text{s}$ following the trigger pulse of 0.178 ± 0.003 and a number of correlated avalanches per pulse in the same time window equal to 0.161 ± 0.005 , also consistent with nEXO requirements. Finally, the PDE of the Hamamatsu VUV4 was measured for two different devices (labeled as VUV4 #2 and VUV4 #1) at $T = 233$ K. At 3.6 ± 0.2 V and 3.5 ± 0.2 V of over voltage we measure, for a mean

wavelength of 189 ± 7 nm, a PDE of 13.4 ± 2.6 % and 11 ± 2 % for the two devices, corresponding to a saturation PDE of 14.8 ± 2.8 % and 12.2 ± 2.3 %, respectively. Both values are well below the 24 % saturation PDE advertised by Hamamatsu [33].⁷ More generally, the VUV4 #1 at 3.5 V of over voltage is below the nEXO PDE requirement. The VUV4 #2 instead yields a PDE that is marginally close to meeting the nEXO specifications. This suggests that with modest improvements the Hamamatsu VUV4 MPPCs could be considered as an alternative to the FBK-LF SiPMs for the design of the nEXO detector.

Acknowledgments

This work has been supported by NSERC, Canada, CFI, Canada, FRQNT, Canada, NRC, Canada, and the McDonald Institute (CFREF) in Canada; by the Offices of Nuclear and High Energy Physics within DOE's Office of Science, and National Science Foundation in the United States; by SNF in Switzerland; by Institute for Basic Sciences in Korea; by RFBR (18-02-00550) in Russia; and by CAS and ISTCP in China. This work was supported in part by Laboratory Directed Research and Development (LDRD), USA programs at Brookhaven National Laboratory (BNL), Lawrence Livermore National Laboratory (LLNL), USA, Oak Ridge National Laboratory (ORNL), USA, and Pacific Northwest National Laboratory (PNNL), USA.

References

- [1] E. Garutti, Silicon photomultipliers for high energy physics detectors, *J. Instrum.* 6 (10) (2011) C10003.
- [2] L. Baudis, M. Galloway, A. Kish, C. Marentini, J. Wulf, Characterisation of silicon photomultipliers for liquid xenon detectors, *J. Instrum.* 13 (10) (2018) P10022.
- [3] nEXO Collaboration, S. Al Kharusi, et al., nEXO Pre-Conceptual Design Report, 2018, arXiv:1805.11142.
- [4] I. Ostrovskiy, F. Retière, D. Auty, J. Dalmasson, T. Didberidze, R. DeVoe, G. Gratta, L. Huth, L. James, L. Lupin-Jimenez, N. Ohmart, A. Piepke, Characterization of silicon photomultipliers for nEXO, *IEEE Trans. Nucl. Sci.* 62 (4) (2015) 1825–1836.
- [5] DarkSide Collaboration, C.E. Aalseth, et al., DarkSide-20k: A 20 tonne two-phase LAr TPC for direct dark matter detection at LNGS, *Eur. Phys. J. Plus* 133 (3) (2018) 131.
- [6] nEXO Collaboration, J.B. Albert, et al., Sensitivity and discovery potential of the proposed nEXO experiment to neutrinoless double- β decay, *Phys. Rev. C* 97 (6) (2018) 065503.
- [7] nEXO Collaboration, A. Jamil, et al., VUV-sensitive silicon photomultipliers for xenon scintillation light detection in nEXO, *IEEE Trans. Nucl. Sci.* 65 (11) (2018) 2823–2833.
- [8] K. Fujii, Y. Endo, Y. Torigoe, S. Nakamura, T. Haruyama, K. Kasami, S. Mihara, K. Saito, S. Sasaki, H. Tawara, High-accuracy measurement of the emission spectrum of liquid xenon in the vacuum ultraviolet region, *Nucl. Instrum. Methods Phys. Res. A* 795 (2015) 293–297.
- [9] L. Fabris, Novel readout design criteria for sipm-based radiation detectors, 2015, https://aisberg.unibg.it/retrieve/handle/10446/52227/107791/Binder_Fabris_DT.pdf.
- [10] F. Arneodo, M.L. Benabderrahmane, G. Bruno, V. Conicella, A. Di Giovanni, O. Fawwaz, M. Messina, A. Candela, G. Franchi, Cryogenic readout for multiple vuv4 multi-pixel photon counters in liquid xenon, *Nucl. Instrum. Methods Phys. Res. A* 893 (2018) 117–123.
- [11] <https://www.omega.com>.
- [12] <https://www.hamamatsu.com>.
- [13] <https://www.knightoptical.com>.
- [14] <https://www.esourceoptics.com>.
- [15] <https://www.newport.com>.
- [16] CAEN, Waveform Recording Firmware Register, <https://www.caen.it/products/dt5730/>.
- [17] MIDAS Collaboration, Maximum Integrated Data Acquisition System, <https://midas.triumf.ca>.
- [18] <http://www.minicircuits.com/pdfs/MAR-6SM+.pdf>.
- [19] <http://www.pelhamresearchoptical.com>.
- [20] <http://resonance.on.ca>.
- [21] R. Brun, F. Rademakers, ROOT an object oriented data analysis framework, *Nucl. Instrum. Methods Phys. Res. A* 389 (1–2) (1997) 81–86.
- [22] Y. Du, F. Retière, After-pulsing and cross-talk in multi-pixel photon counters, *Nucl. Instrum. Methods Phys. Res. A* 596 (3) (2008) 396–401.
- [23] F. Corsi, C. Marzocca, A. Perrotta, A. Dragone, M. Foresta, A. Del Guerra, S. Marcatili, G. Llosa, G. Collazuol, G.F. Dalla Betta, N. Dinu, C. Piemonte, G.U. Pignatelli, G. Levi, Electrical characterization of silicon photo-multiplier detectors for optimal front-end design, in: *IEEE Nuclear Science Symposium Conference Record*, IEEE, 2006, pp. 1276–1280.
- [24] F. Retière, Y. Du, S. Foreman, P. Kitching, A. Kostin, T. Lindner, M. Low, P. Masliah, I. Moul, S. Oser, H. Tanaka, A. Vacheret, Characterization of multi pixel photon counters for T2K near detector, *Nucl. Instrum. Methods Phys. Res. A* 610 (1) (2009) 378–380.
- [25] A.N. Otte, D. Garcia, T. Nguyen, D. Purushotham, Characterization of three high efficiency and blue sensitive silicon photomultipliers, *Nucl. Instrum. Methods Phys. Res. A* 846 (2017) 106–125.
- [26] A. Ghassemi, K. Sato, K. Kobayashi, MPPC, Hamamatsu Technical Note, KAPD9005E01, 2017, pp. 1–65, https://www.hamamatsu.com/resources/pdf/ssd/mppc_kapd9005e.pdf.
- [27] <http://www.waynekerrtest.com/index.php>.
- [28] G.A.M. Hurkx, H.C. de Graaff, W.J. Kloosterman, M. Knuvers, A new analytical diode model including tunneling and avalanche breakdown, *IEEE Trans. Electron Devices* 39 (9) (1992) 2090–2098.
- [29] J. Rosado, V.M. Aranda, F. Blanco, F. Arqueros, Modeling crosstalk and afterpulsing in silicon photomultipliers, *Nucl. Instrum. Methods Phys. Res. A* 787 (2015) 153–156.
- [30] F. Acerbi, S. Davini, A. Ferri, C. Galbiati, G. Giovanetti, A. Gola, G. Korga, A. Mandarano, M. Marcante, G. Paternoster, C. Piemonte, A. Razeto, V. Regazzoni, D. Sablone, C. Savarese, G. Zappala, N. Zorzi, Cryogenic characterization of FBK HD near-UV sensitive SiPMs, *IEEE Trans. Electron Devices* 64 (2) (2017) 521–526.
- [31] A. Butcher, L. Doria, J. Monroe, F. Retière, B. Smith, J. Walding, A method for characterizing after-pulsing and dark noise of PMTs and SiPMs, *Nucl. Instrum. Methods Phys. Res. A* 875 (2017) 87–91.
- [32] H. Photonics, Photomultiplier tubes, basics and applications, 2007, https://www.hamamatsu.com/resources/pdf/etd/PMT_handbook_v3aE.pdf.
- [33] K. Yamamoto, R. Yamada, K. Kobayashi, K. Sato, A. Ghassemi, New improvements to a specialized multi-pixel photon counter (MPPC) for neutrinoless double-beta decay and dark matter search experiments, 2016, ICHEP, ID:450 https://www.hamamatsu.com/sp/ssd/microsite/MPPC/ICHEP_MPPC_panel_160731.pdf.
- [34] <https://geant4.web.cern.ch>.
- [35] G. Collazuol, M.G. Bisogni, S. Marcatili, C. Piemonte, A. Del Guerra, Studies of silicon photomultipliers at cryogenic temperatures, *Nucl. Instrum. Methods Phys. Res. A* 628 (1) (2011) 389–392.
- [36] E.B. Johnson, X.J. Chen, R. Miskimen, D. Von Maluski, C.J. Stapels, S. Mukhopadhyay, F. Augustine, J.F. Christian, Characteristics of CMOS avalanche photodiodes at cryogenic temperatures, in: *IEEE Nuclear Science Symposium Conference Record*, vol. 92024, IEEE, 2009, pp. 2108–2114.
- [37] Si EUV Photodiode Transfer Standard, <https://www.nist.gov/laboratories/tools-instruments/si-euv-photodiode-transfer-standard>.
- [38] O. Girard, G. Haefeli, A. Kuonen, L. Pescatore, O. Schneider, M.E. Stramaglia, Characterisation of silicon photomultipliers based on statistical analysis of pulse-shape and time distributions, 2018, <http://arxiv.org/abs/1808.05775>.

⁷ This discrepancy could be related to the different technique used by Hamamatsu to evaluate the VUV4 PDE. Accordingly to an internal meeting with Hamamatsu the PDE reported in [33] was not assessed by pulse counting, but reading out instead the MPPC current under illumination. However, as shown in [38], the MPPC current is affected by CA noise and it is therefore easier to overestimate the PDE if the CA noise contribution is not accounted properly.